Kim, H. K., Shterenlikht, A., Pavier, M. J., Velichko, A., & Alexander, N. A. (2016). On stability of a new side cut destructive method for measuring non-uniform residual stress in thin plates. *International Journal of Solids and Structures*, *100-101*, 223–233. https://doi.org/10.1016/j.ijsolstr.2016.08.019

On stability of a new side cut destructive method for measuring non-uniform residual stress in thin plates

H. K. Kim*, A. Shterenlikht, M. J. Pavier, A. Velichko, N. A. Alexander

Department of Mechanical Engineering, University of Bristol, Queen's Building, University Walk, Bristol BS8 1TR, UK

Abstract

Stability and sensitivity analyses of a recently proposed mechanical strain relaxation method for residual stress measurement in thin plates are presented. The method is based on the Mathieu series solution for a semi-infinite elastic strip with self-equilibrated end loading. The effects of the specimen length, incomplete displacement data and rigid body rotation errors were analysed. The results of this analysis were applied to improve the performance of the method for the measurement of the residual stress in a 3 mm thick friction stir welded plate of Aluminium 5083-O alloy. A through cut was introduced with an electrical discharge machining (EDM) wire. 3D digital image correlation was used to measure the relaxation displacements. The reconstructed residual stress profile agrees with that measured by energy dispersive X-ray diffraction (EDXRD). It is shown that the orientation of the EDM wire with respect to the plate significantly affects cutting induced plastic strain. This strain is minimised when the EDM cut is through the thickness of the plate, i.e. when the plate width direction is parallel to the EDM wire. Such orientation of the EDM wire leads to a minimal induced-plasticity on the cut surface. This is a major strength of the method, which makes it attractive in practical applications where other mechanical stress relaxation methods suffer from plastic flow on cutting.

Keywords: Non-uniform residual stress, Digital image correlation, Friction stir welding, Mechanical strain relaxation, Inverse problems, Plasticity

*Corresponding author

Email address: hk.kim@bristol.ac.uk (H. K. Kim)

1. Introduction

Many non-destructive and destructive residual stress (RS) measurement techniques are used successfully in a great variety of engineering applications. Neutron diffraction [1, 2], synchrotron X-ray [3, 4] and lab X-ray diffraction [5] are the most commonly used non-destructive methods. These methods are based on measuring inter-atomic distances in stressed and unstressed material and converting those to strain [6].

Destructive (mechanical stress relaxation or MSR) techniques measure strain or displacement caused by removal of some material. The measured relaxation is converted to stress using a range of elastic models [7]. The popular techniques include hole drilling [8], deep hole drilling [9], slitting [10, 11] and contour methods [12].

Although these techniques have been successful, they have limitations. Diffraction methods work only with crystalline materials and require expensive facilities for subsurface measurement. Quality of hole drilling RS measurements critically depends on stress uniformity within several hole diameters [13], so it cannot be used on RS fields with high gradients. In addition, to capture rapidly changing fields, many holes and many strain gauges are required, which increases the complexity and costs of experiments [14]. The slitting method [11, 10, 15] can be used if the RS field is non-uniform along the slit depth, though it must be uniform along the the slit width. In addition, high uncertainty is expected for near surface measurements [11].

Recently, a new MSR technique has been proposed [16]. It is designed specifically for the measurement of RS measurement in plates, where RS can be highly non-uniform in-plane, but constant through thickness. The method involves a single cut at the midsection of the longitudinal direction of the plate, propagated either (i) through the thickness of the plate, called the 'side cut', or (ii) through the width of the plate, called the 'top cut'. Full-field relaxation displacements from the side surface are recorded with 3D digital image correlation (DIC). An elastic analytical model was used to convert the relaxation displacements into stresses using standard inverse method procedures. The technique was shown to be relatively insensitive to random displacement measurement errors and successfully implemented to measure the RS generated by four-point bending in a bar of square cross section [16].

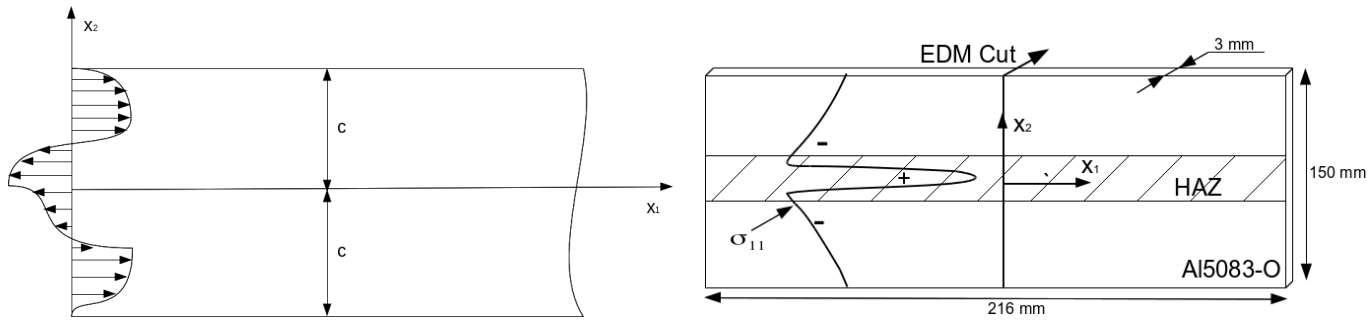

(a) (b)

Figure 1: (a) The problem geometry for a 2D semi-infinite rectangular strip, of width $2c$, with arbitrary self-equilibrated end load [16]. (b) The friction stir welding (FSW) specimen used in this work. The specimen is cut with wire EDM at $x_1 = 0$, the symmetry plane.

In this work, further error analysis was carried out to improve the performance of the method. The method was then applied to measure the RS field in a thin friction stir welding (FSW) plate. This application was chosen because the method has unique advantages when used on thin plates with non-uniform in-plane RS fields. Applications of most other MSR methods to thin plates can suffer from global plate distortion [17, 18], which makes precise relaxation measurement hard, resulting in higher measurement errors [19]. It is shown that RS measured in the FSW plate with the new method, refined following the sensitivity and stability analysis, agrees with that measured by energy dispersive X-ray diffraction (EDXRD) in prior work [20]. It is also shown that using the side cut introduces little or no plastic strain, which can be a problem in other MSR methods.

2. The analytical model

For a detailed description of the analytical solution the reader is referred to [16, 21]. A brief overview is given here.

The Mathieu series solution for a 2D semi-infinite strip of width $2c$ with arbitrary self-equilibrated loading at the end was used [22], see Fig. 1(a). A combination of the following even, f, and odd, g, (with respect to x_2) stress functions was used:

$$f_i = e^{-\gamma_i x_1/c}\left(\xi_i \cos\frac{\gamma_i x_2}{c} + \frac{\gamma_i x_2}{c}\sin\frac{\gamma_i x_2}{c}\right); \qquad g_i = e^{-\phi_i x_1/c}\left(\psi_i \sin\frac{\phi_i x_2}{c} + \frac{\phi_i x_2}{c}\cos\frac{\phi_i x_2}{c}\right) \quad (1)$$

The boundary conditions are $\sigma_{22} = \sigma_{12} = 0$ at $x_2 = \pm c$ and $\int_{-c}^{c} \sigma_{22} \mathrm{d}x_2 = \int_{-c}^{c} \sigma_{12} \mathrm{d}x_2 = 0$ at $x_1 = 0$, see Fig. 1(a), which lead to the following constraints:

$$\sin 2\gamma_i + 2\gamma_i = 0; \qquad \xi = -\gamma_i \tan \gamma_i; \qquad \sin 2\phi_i - 2\phi_i = 0; \qquad \psi = -\phi_i / \tan \phi_i \tag{2}$$

which have infinite number of solutions for dimensionless $\gamma_i, \xi_i, \phi_i, \psi_i$. A complete stress function, suitable for any arbitrary self-equilibrated stress on the boundary, is constructed as follows:

$$\theta = \sum_{i=1}^{\infty} a_i \Re(f_i) + b_i \Im(f_i) + c_i \Re(g_i) + d_i \Im(g_i) \tag{3}$$

By selecting coefficients of a_i, b_i, c_i and d_i, any arbitrary self-equilibrated loading at the $\mathrm{x}_1 = 0$ boundary can be constructed. The forward stress solution is then immediately obtained. An inverse solution can be constructed for known displacement fields. Using plane stress, small strain and linear isotropic elasticity assumptions, the surface in-plane displacements can be expressed as follows:

$$\begin{aligned}
Eu_1 = \quad & \sum_{i=1}^{\infty} a_i \int \Re\left(\frac{\partial^2 f_i}{\partial x_2^2} - \nu \frac{\partial^2 f_i}{\partial x_1^2}\right) dx_1 + b_i \int \Im\left(\frac{\partial^2 f_i}{\partial x_2^2} - \nu \frac{\partial^2 f_i}{\partial x_1^2}\right) dx_1 \\
& + c_i \int \Re\left(\frac{\partial^2 g_i}{\partial x_2^2} - \nu \frac{\partial^2 g_i}{\partial x_1^2}\right) dx_1 + d_i \int \Im\left(\frac{\partial^2 g_i}{\partial x_2^2} - \nu \frac{\partial^2 g_i}{\partial x_1^2}\right) dx_1 \\
Eu_2 = \quad & \sum_{i=1}^{\infty} a_i \int \Re\left(\frac{\partial^2 f_i}{\partial x_1^2} - \nu \frac{\partial^2 f_i}{\partial x_2^2}\right) dx_2 + b_i \int \Im\left(\frac{\partial^2 f_i}{\partial x_1^2} - \nu \frac{\partial^2 f_i}{\partial x_2^2}\right) dx_2 \\
& + c_i \int \Re\left(\frac{\partial^2 g_i}{\partial x_1^2} - \nu \frac{\partial^2 g_i}{\partial x_2^2}\right) dx_2 + d_i \int \Im\left(\frac{\partial^2 g_i}{\partial x_1^2} - \nu \frac{\partial^2 g_i}{\partial x_2^2}\right) dx_2
\end{aligned} \tag{4}$$

By truncating the series limit at n, the unknown coefficients a_i, b_i, c_i, d_i, are found from the solution of the standard linear least square (LLS) problem:

$$\min_x ||\mathbf{A}\mathbf{x} - \mathbf{u}||_2 \tag{5}$$

where $\mathbf{x}$ is the vector of $4n$ unknown series coefficients, $\mathbf{u}$ is a vector of $2m$ displacement values, $\mathbf{A}$

is a $2m \times 4n$ matrix of integral functions taken at the location of each of the measurement points. To improve LLS stability, the number of measured displacement points, m, should be considerably higher than the number of terms in the series expansion, n. In practice, hundreds or thousands of data points are needed, which means the method requires a full-field measurement technique, such as DIC.

Tikhonov regularisation of the LLS problem was implemented to improve stability [23, 24, 25]. Eigenvalues smaller than 0.01 of the largest eigenvalue were set to 0. This transforms the problem into finding a minimum norm solution to the inverse problem. LAPACK LLS routines [26] were used.

3. Error analysis

Prior work showed that the reconstructed RS profile suffered from significant noise [16], which is believed to be the cumulative result of various experimental errors. A detailed analysis of the influence of a range of experimental errors on the reconstructed RS profile is given here.

Four types of input error are likely to be introduced in an experiment. Random errors include (1) random displacement noise and (2) missing data, e.g. due to failed DIC pattern. Systematic errors include (3) insufficient length of the specimen and (4) rigid body rotation. Previous error analysis concluded that the method was relatively insensitive to random noise in experimental displacements [16]. Errors associated with missing data and systematic errors are investigated in detail in this section.

3.1. Effect of specimen length

The analytical solution is based on a semi-infinite plate. Applying this solution to a specimen of finite length is adequate as long as the specimen is long enough such that the relaxation caused by the cutting is fully contained within the specimen and does not reach the far end. The purpose of this analysis is to find out the effect of the specimen length if it is too short.

The Abaqus 6.12 FE package [27] was used for this study. A 2D plane stress model of the half length of the plate was used, exploiting symmetry on $x_1 = 0$, see Fig. 2(a). The size of the model was 106 mm $\times$ 150 mm. Isotropic linear elasticity was used with the Young's modulus of 71

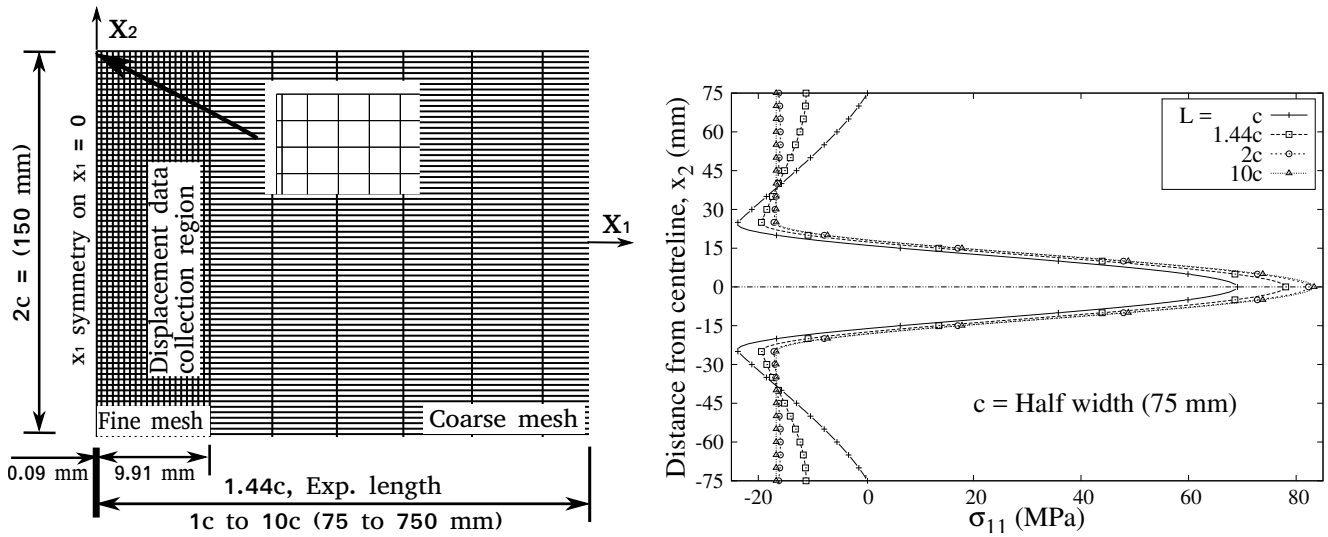

Figure 2: (a) Schematic of the 2D FE model. The different lengths of the model have been generated from $1c$ to $10c$. The elements on the left edge are 0.09 mm by 0.5 mm. Cutting was simulated via element removal. For the reconstruction, displacement data was collected from the nodes in the fine mesh region, $x_1 = 0.09$ to 10 mm. The inset shows a magnified view of the top left corner of the model. (b) Shapes of RS fields, after stress equilibration, obtained from the FE models of different lengths.

GPa and the Poisson's ratio of 0.33. Isotropic power hardening plasticity was used with the yield stress of 145 MPa and the UTS of 290 MPa. These values were chosen to represent Aluminium 5083-O, the experimental material chosen for this study. The hardening data was obtained from [20]. Bell shaped RS fields, expected in thin FSW plates, were chosen for this work. The RS field was simulated using SIGINI Abaqus subroutine [27]. $\sigma_{11} = 100$ MPa was applied between $x_2 = -25$ and $x_2 = 25$ mm. Enforcing stress equilibrium resulted in a residual stress field similar to that in the welding process, see Fig.2(b). The shapes of RS fields change with the length of the FE model. Models of length $L = c, 1.44c, 2c$ and $10c$ were investigated. $L = 1.44c$ was chosen to match the length of the FSW welding specimen available for this work.

22,500 four-node linear elements were used. Three element sizes were used, see 2(a). The smallest elements, 0.09 mm $\times$ 0.50 mm were used to simulate cutting via an element removal technique. These elements were removed instantaneously, causing no plastic strain in the rest of the model. The element size in the data collection region was 0.50 mm $\times$ 0.50 mm, except for a layer of the elements very close to the elements to be cut was 0.41 $\times$ 0.50 mm. The relaxation

displacement data was collected on the region between $x_1 = 0.09$ and 10.00 mm. It was used to reconstruct the RS fields, see Fig. 4. For the rest of the model, the mesh was biased along x_1. A total of 54 nodes were used between $x_1 = 10$ mm and the end of the model. The width of all elements was 0.50 mm. The right edge top and bottom nodes were fixed to avoid rigid body motion.

Fig. 3 shows the relaxation displacement fields from the model of length $10c$. u_1 and u_2 drop to zero by about about $x_1 = 2c$. If the specimen is shorter than $2c$, then the u_1 and u_2 fields will not match the analytical model, which assumes $u_1 = u_2 = 0$ only at $x_1 \to +\infty$. Using displacement data from short specimens will result in incorrectly reconstructed series expansion coefficients. In particular, higher order anti-symmetric terms, which are zero for symmetric RS fields, become substantially different from zero, producing high oscillations seen in the RS profile.

The RS fields from different lengths of the model were reconstructed with the series expansion limit of 15, see Fig. 4. As expected, shorter models result in higher error.

If the specimen is longer than $2c$, then the boundary conditions on the free end of the plate are not important, because the right edge is guaranteed to be stress free, i.e. zero reaction forces. However, for shorter specimens, the boundary condition type becomes important.

Two types of right edge constrains were analysed with short FE models: (1) far edge top and bottom nodes are fixed, and (2) far edge fixed bottom node and $u_1 = 0$ at the top node. It appears that fixing both corners gives a lower error, see Fig. 4(b).

Fig. 5 shows that clamping at $x_1 = 0.933$c has a small effect on the reconstructed RS profile. The location of the clamp is shown in Fig. 3(a). This location for the clamp was later used in the experiment.

3.2. Sensitivity to limited displacement data

Previous work considered the case when a few displacement data points are missing at the cut edge of the specimen [16]. In this work we analyse more severe cases: (1) displacements are available only from half width of the specimen. and (2) u_2 displacement data are set to zero due to poor quality of this data. The first case can typically arise when the RS field is known in advance to be symmetric with respect to x_2. Reducing the field of view to half the width then allows one

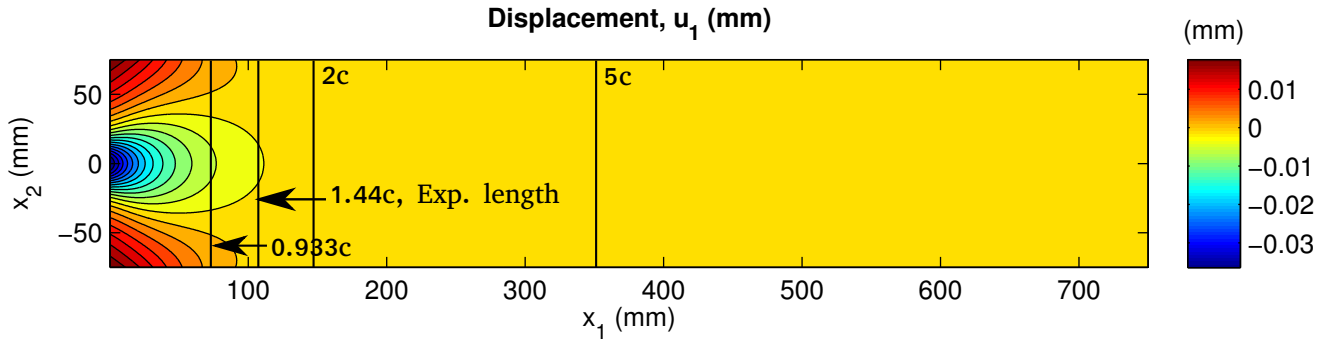

(a)

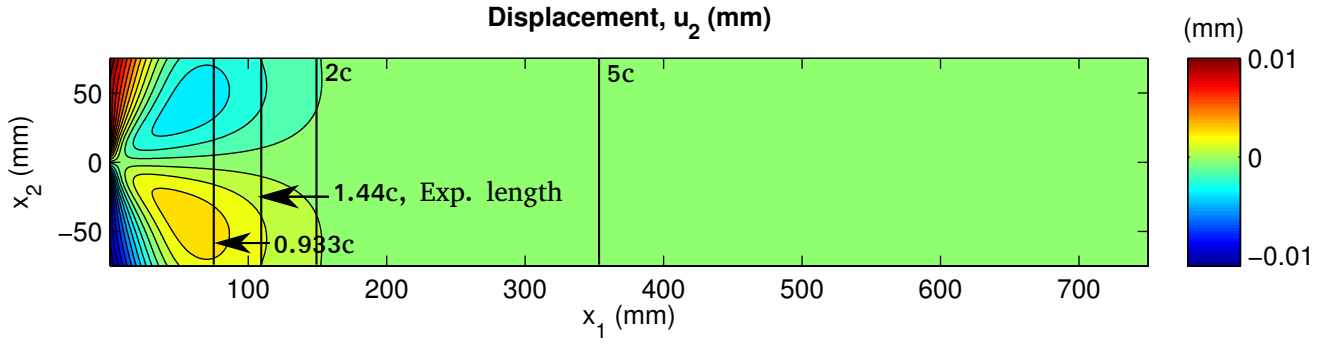

(b)

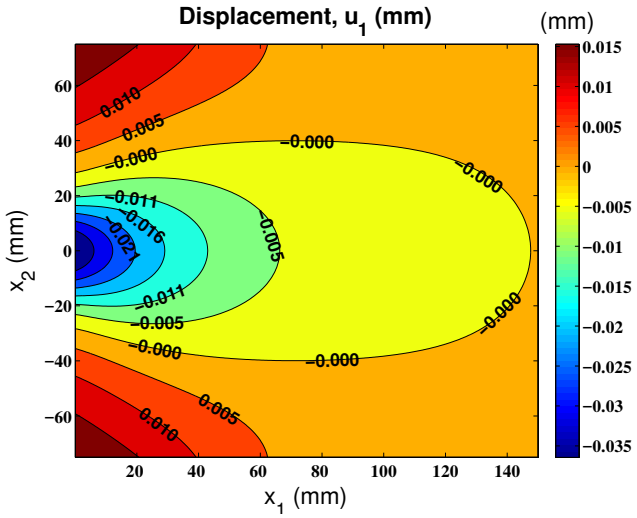

(c)

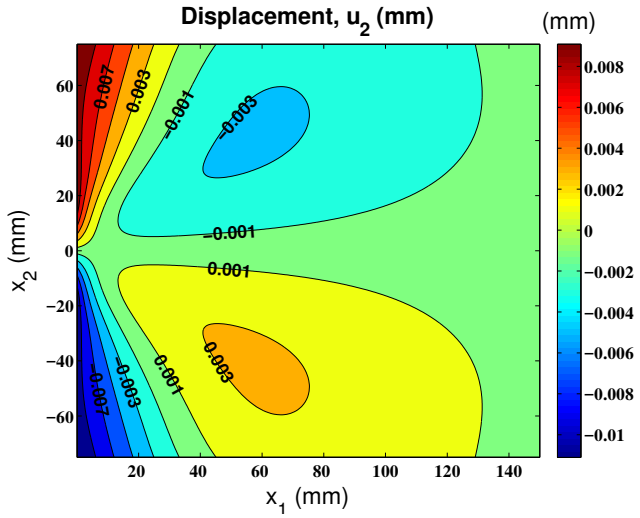

(d)

Figure 3: The relaxation displacement fields, showing (a) u_1 and (b) u_2 obtained from the 2D plain stress FE model. The width was $2c = 150$ mm and the length was $10c = 750$ mm. (c) and (d) show u_1 and u_2 in the region between $x_1 = 0$ and $2c$. Different lengths of the models have been generated which are indicated in (a) and (b). The stress fields, reconstructed from each model are shown in Fig. 4.

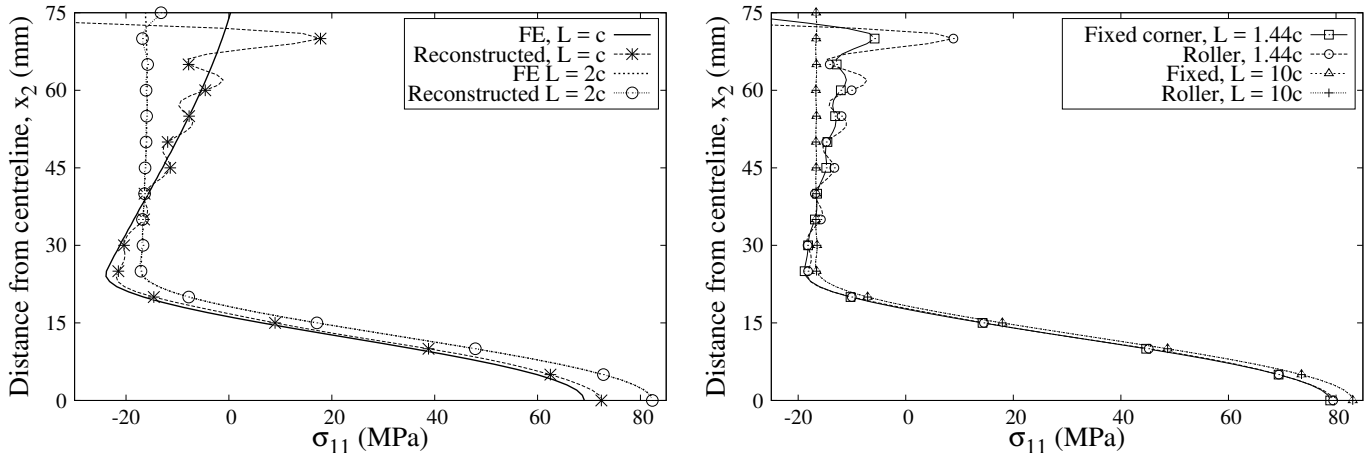

Figure 4: Reconstructed RS profiles in FE models with $L = 1c$ and $2c$. The series expansion limit was 15. Agreement improves with increasing model length. Only half width of the stress fields were presented due to the symmetry condition. (a) Effect of different free end constraints on reconstructed stresses. While for long model, $L = 10c$, constraint type makes no difference, for $L = 1.44c$, two fixed right edge corners give better match.

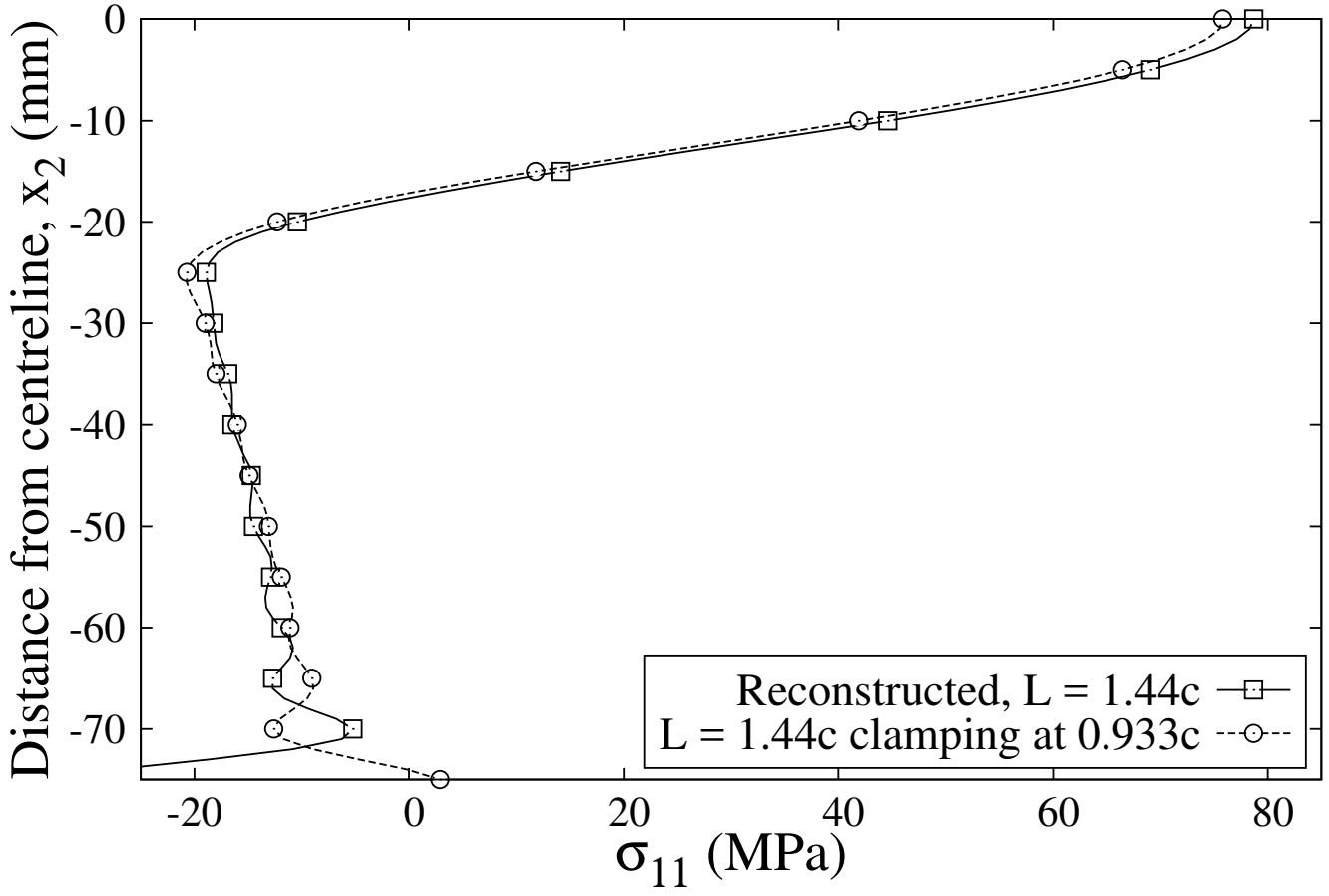

Figure 5: Effects of clamping for the $L = 1.44c$ model.

	a_i	b_i
1	2.29×10^{0}	3.97×10^{0}
2	7.08×10^{-1}	4.69×10^{-1}
3	2.22×10^{-1}	1.26×10^{-1}
4	6.80×10^{-2}	3.94×10^{-2}
5	1.71×10^{-2}	1.26×10^{-2}
6	8.88×10^{-4}	3.23×10^{-3}
7	-2.07×10^{-3}	-8.97×10^{-5}
8	-8.57×10^{-4}	-5.94×10^{-4}
9	4.05×10^{-5}	-1.64×10^{-4}
10	3.04×10^{-5}	3.84×10^{-5}

(a)

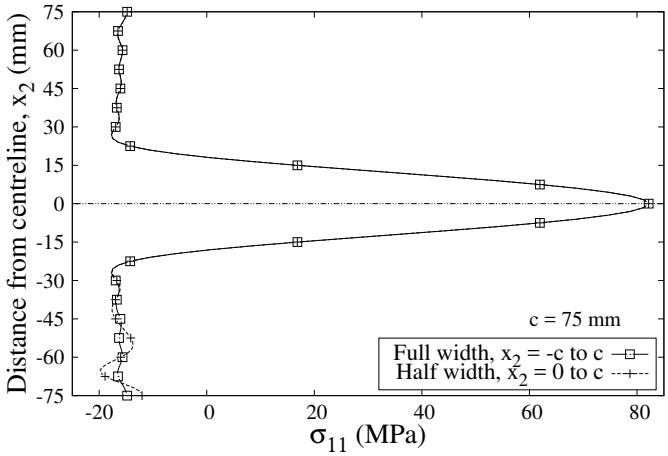

(b)

Figure 6: (a) 10 first terms in the series expansion in Eqn. (3) used for the forward solution. Due to RS symmetry, odd terms (c_i and d_i) were set to zero. (b) Reconstructed RS profiles using the half and the full width. The half width reconstruction is worse for $x_2 < 0$, where the data was not collected.

to increase the spatial resolution by a factor of 2. The second case is important because relaxation along x_2 is only due to the Poisson's effect. Hence u_2 is typically about 3 times smaller than u_1. Hence u_2 suffers from worse signal to noise ratio compared to u_1.

The inverse solution used as input the displacements calculated analytically using the forward solution with pre-set series expansion coefficients, a_i, b_i, c_i, d_i, see Eqn. 3. Before using the inverse solution, the analytical displacements were perturbed randomly and systematically to assess the sensitivity of the inverse solution.

The $L = 2c$ model was used in this analysis. The first 10 terms in the series expansion were calculated from the FE model, described in Sec. 3.1. These are listed in Fig. 6(a), which shows only the even terms, a_i, b_i. The odd terms are zero because the RS field is symmetric.

Fig. 7(a) compares the reconstructed RS profiles, obtained using displacement data from different collection regions, from $x_2 = -c$ to $0.5c$ and c, against the applied RS. FE model of length $2c$ was used. There is a very good match between the forward and the reconstructed RS field, obtained from full width data ($x_2 = -c$ to c). When the data collection window is reduced, the match becomes worse. When the data is collected from only half the width, a good match is obtained only where data is available, see Fig. 6(b). Using only u_1 displacement data in the the

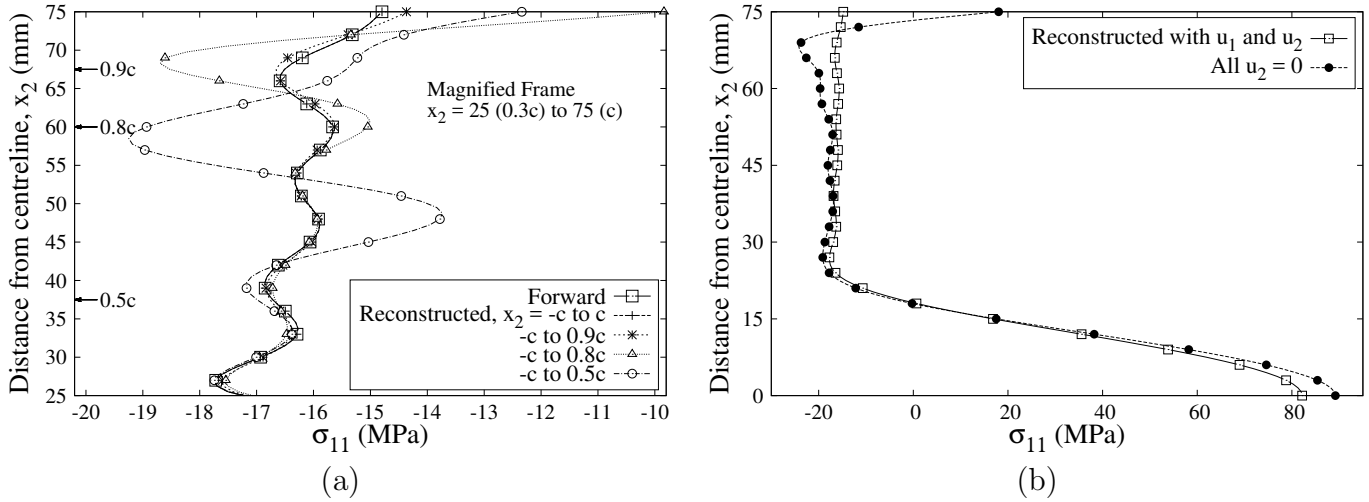

Figure 7: (a) RS profiles, reconstructed using the relaxation displacements from different regions, from $x_2 = -c$ to $0.5c$ and c, compared with the applied RS profile. The applied RS was calculated using the series expansion coefficients in Fig. 6(a). (b) Inverse stress profiles reconstructed with and without u_2 displacement data.

analytical solution results in a worse inverse solution, see Fig. 7(b).

3.3. Rigid body rotation

The stress distribution used in Sec. 3.1 was used in a 2D FE model with $L = 2c$ to calculate the relaxation displacements similar to those in Fig. 3(c-d). A rigid body rotation of 0.01° about the origin, $x_1 = 0, x_2 = 0$, changes displacements dramatically as shown in Fig. 8. In this example, the value of 0.01° was chosen because it gives the artificial displacement, due to the rotation, of the same order as the magnitude of the maximum u_1. Thus, the maximum magnitude of u_2 displacement due to the rotation is approximately 3 times greater than that without the rotation, see Fig 8(b) and 3(d). In the experiments, clamping was used to reduce the rigid body rotation to below 0.01°. The reconstructed residual stress profiles are shown in Fig. 9. When the rotated displacement fields are used, the reconstructed RS field suffers from high oscillations.

Rigid body compensation is thus required. An approach used previously for the hole drilling method with Electronic Speckle Pattern Interferometry (ESPI) [28] was applied here. Displace-

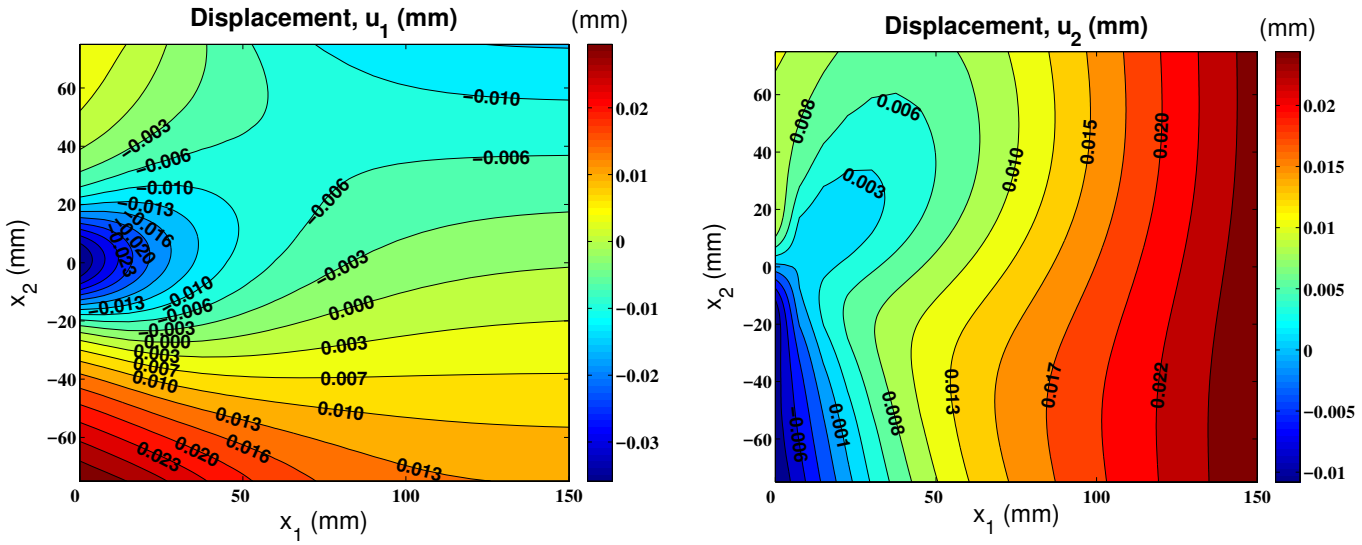

(a) (b)

Figure 8: (a) u_1 and (b) u_2 FE relaxation displacements with added rigid body rotation by 0.01° about $x_1 = 0, x_2 = 0$. $L = 2c$. Other FE model details are shown in Fig. 3(d).

ments due to rigid body motion can be expressed as:

$$\left\{ \begin{array}{c} u_1^M \\ u_2^M \end{array} \right\} = \left\{ \begin{array}{c} u_1^T + u_1^R \\ u_2^T + u_2^R \end{array} \right\} = \left\{ \begin{array}{ccccc} u_1^T & + & (\cos\alpha - 1)x_1 & - & \sin\alpha x_2 \\ u_2^T & + & \sin\alpha x_1 & + & (\cos\alpha - 1)x_2 \end{array} \right\} \tag{6}$$

where superscripts T and R refer to the in-plane translation and rotation accordingly. α is the rotation angle. This displacement was added to Eqn. 4. As a result, the reconstructed RS field agreed very well with the applied RS field, see Fig. 9.

4. Effect of different cutting schedules

A previous FE study [16] showed that propagating the cut from different directions in a four-point bend RS specimen causes different amount of stress redistribution. Significant stress redistribution can lead to plastic deformation during cutting if the magnitude of RS is close to yield. However, it was possible to arrange the EDM wire so that a self-equilibrated RS field was removed on each cutting increment, i.e. $\int_{\Delta A} \sigma_{11} dA = 0$, where ΔA is the area of material removed in each increment of the cut. This reduces residual stress redistribution in the material ahead of the EDM wire, which is a common cause of plastic strain on cutting [16].

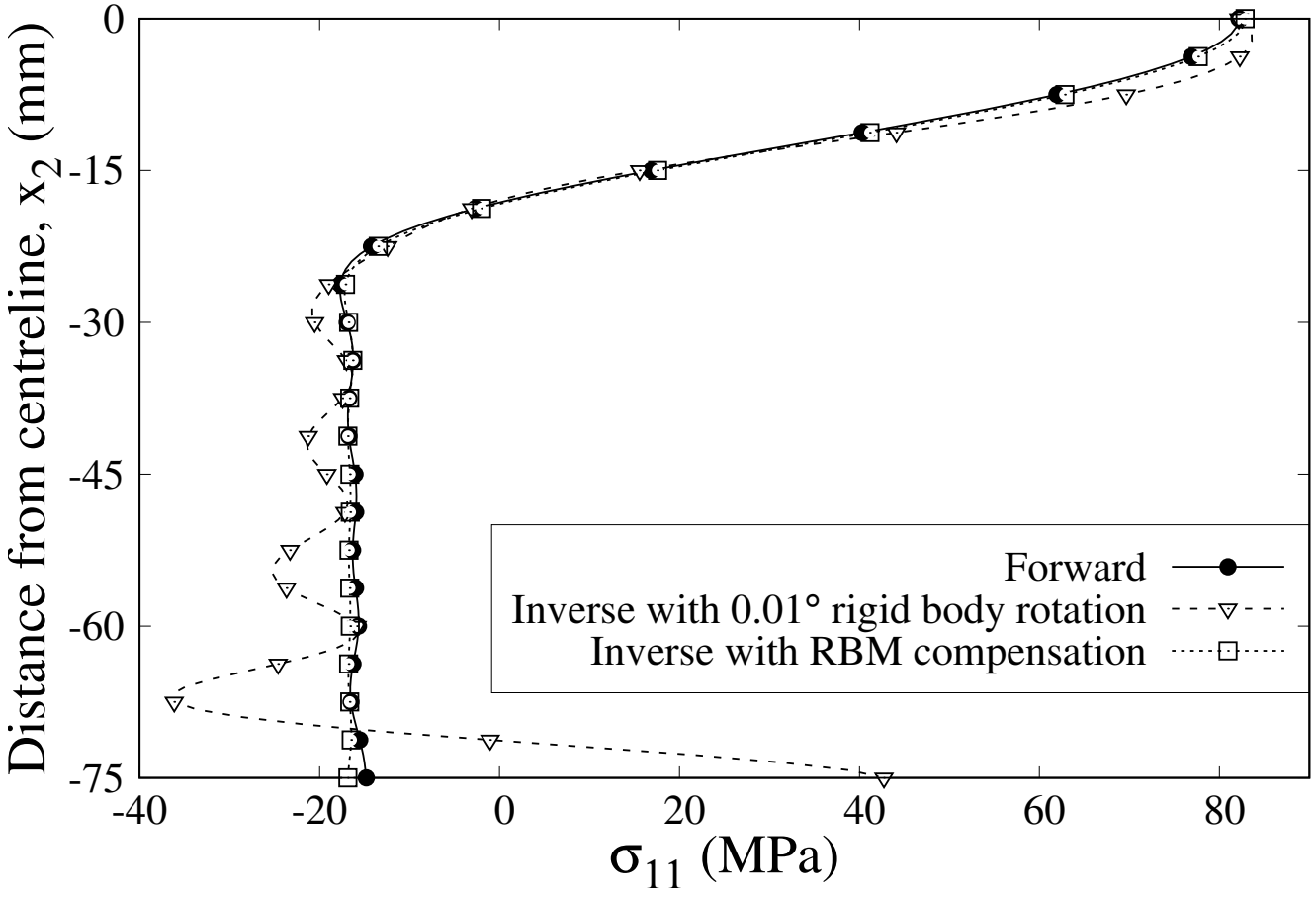

Figure 9: Rigid body motion (RBM) compensation on $L = 2c$ model.

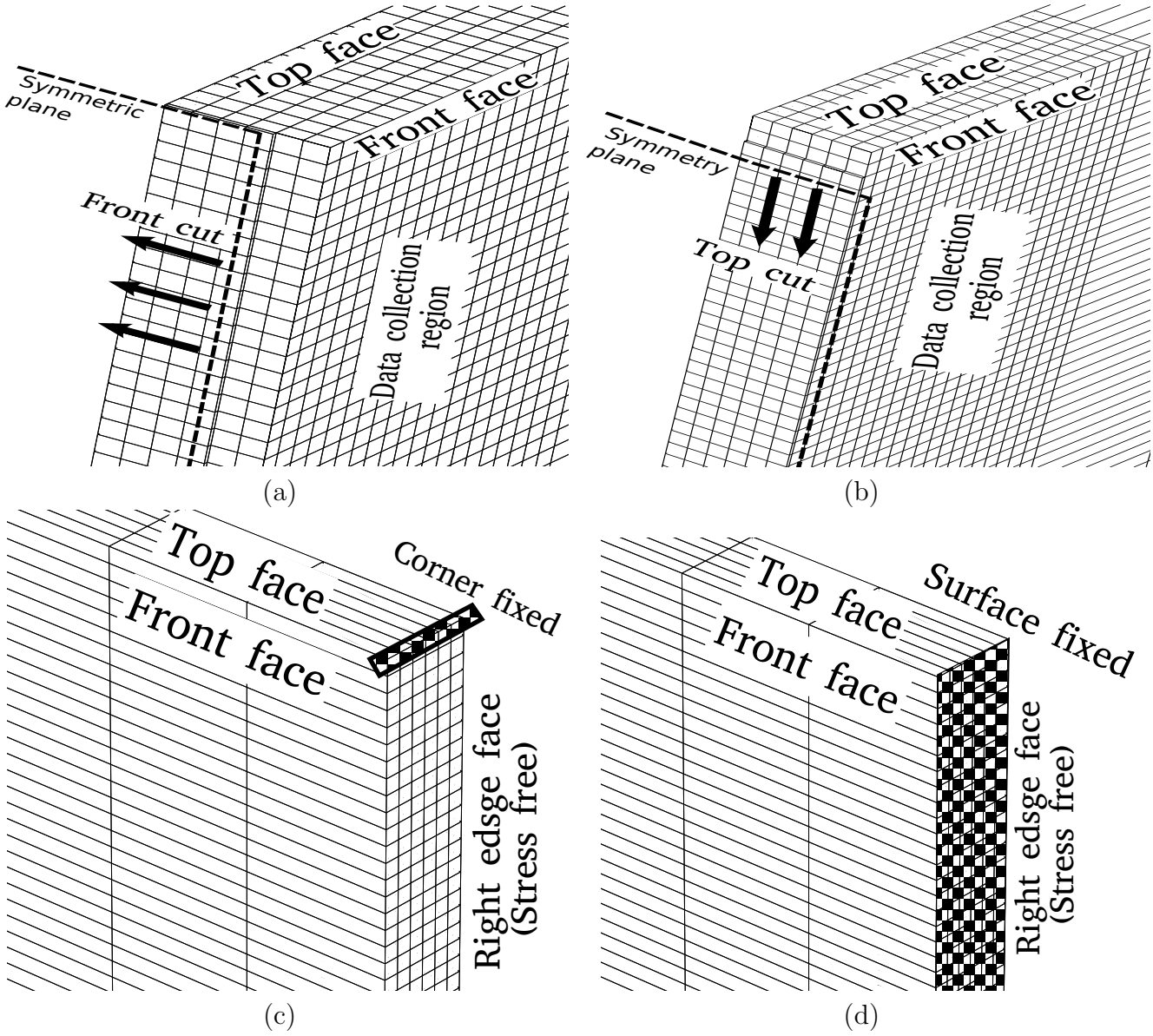

Figure 10: The top near and far corners of 3D FE model (see also Fig. 2(a)). $x_1 = 0$ is the symmetry plane. An incremental cut was simulated by element removal (a) from the top to the bottom face (top cut) and (b) from the front to rear face (side cut). Different constraint were applied at the far end of the model: (c) fixed nodes at the top and the bottom edge, and (d) fixed nodes at the whole end surface.

In this work the conclusions from [16] are applied to a thin plate model. A 108 mm × 150 mm × 3 mm 3D FE model of half plate was used, with symmetry condition on $x_1 = 0$. Applied initial stress and material properties are the same as in the 2D model, see the $1.44c$ case in Fig. 2(b).

73,800 eight-node reduced integration elements were used. The element sizes were 0.5 mm thorough thickness and the same as in the 2D model in plane, see Sec. 3.1. Incremental element removal was used in this model to simulate a progressive cut propagation. Cuts from the top to the bottom, and from the front to the rear side were analysed, see Fig. 10.

The plastic strain fields normal to the cut surface, ϵ^p_{11}, induced by stress redistribution during cutting are shown in Fig. 11. ϵ^p_{11} is shown because it is believed to affect the relaxation displacement on the surface the most. In the top cut with the corner constraint, see Fig. 10(c) there are two plastic peaks, in the regions of x_2 = -8 mm and x_2 = 23 mm, see Fig. 11(a). At these locations plastic strain reaches the front surface, affecting the surface displacements. The peak magnitudes of ϵ^p_{11} are 0.001 and -0.0007. The peaks are not symmetric with respect to x_1 because the locations of the plastic regions are determined by the cumulative effect of RS relaxation. This can be explained quantitatively in terms of K_{Irs}, mode I stress intensity factor resulting from introducing a thin cut into a RS field, [29].

In contrast, in the side cut, see Fig. 11(b) the maximum plastic strain is higher, $\epsilon^p_{11} = 0.0035$, but is located only near the rear face between $x_2 = -10$ and 10 mm.

To see the effect of constraint on induced plasticity, a fixed constraint was applied to two different regions: (1) nodes along the thickness ($x_3 = 0$ to 3 mm) in the top right and bottom right corners (corner constraint), see Fig. 10(c) as it is 2D model in Sec. 3.1, and (2) entire nodes on the right free surface (surface constraint) of the model to avoid rigid body motion, see Fig. 10(d).

For the case of a fixed constraint applied to the whole stress free surface for the top cut model, see Fig. 10(d), the shape of cutting-induced-plasticity on the cut surface is notably changed to a single peak between $x_2 = 0$ and $x_2 = -15$ mm. The magnitude of the peak plastic strain is $\epsilon^p_{11} = 0.002$, which is 2 times higher than the corner constraint case. This suggests that less constraint is preferable, consistent with the slitting method [19]. In contrast, in the contour method high constraint close to the cut is beneficial [30].

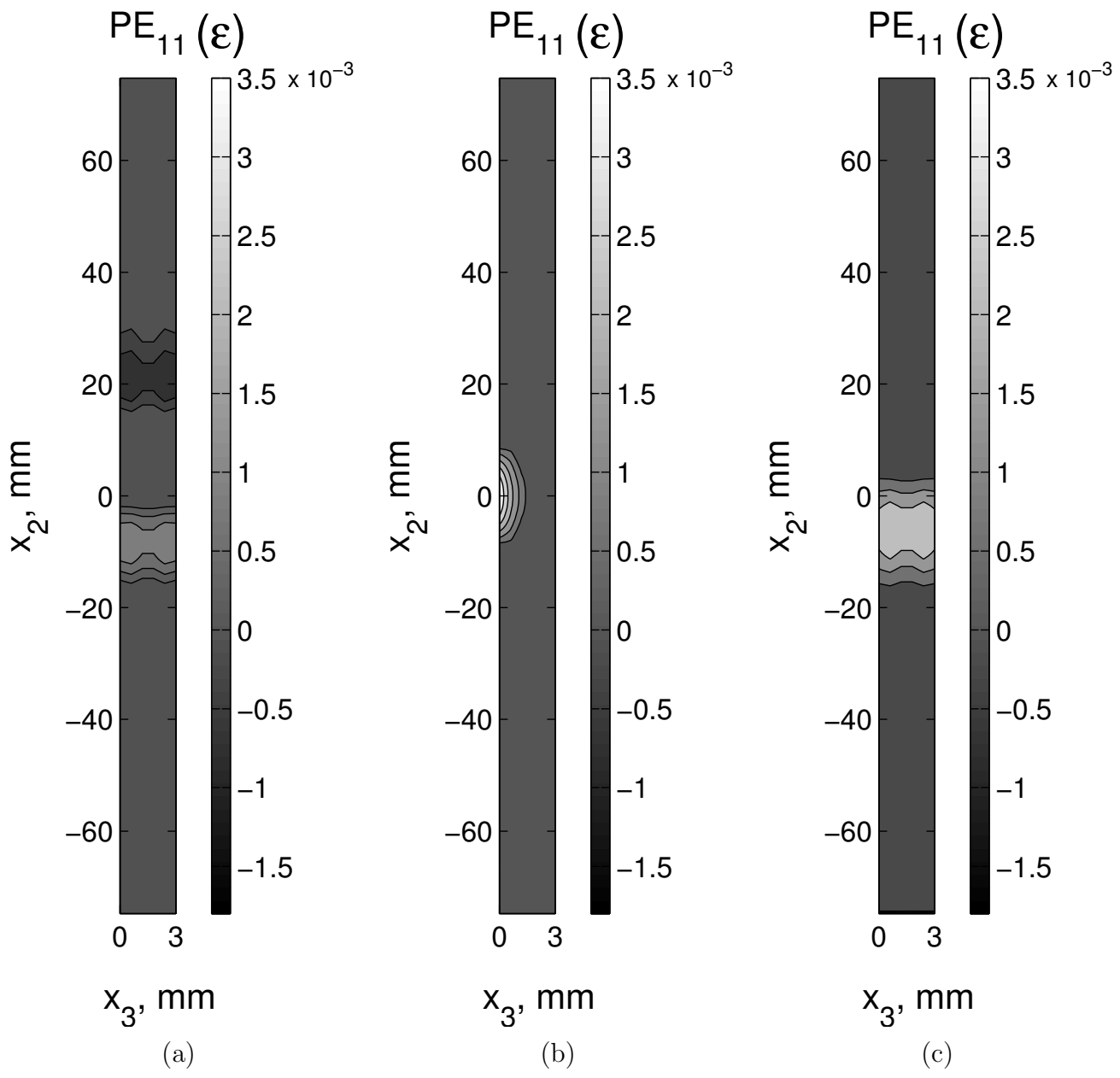

Figure 11: Plastic strain, ϵ_{11}^{p}, on the cut surface resulted from the top cut (a) and from the side cut (b) with the corner constraint. The top cut induces significant plastic strain on the front surface where displacements are measured. In contrast, the side cut leaves no plastic strain on the front surface. (c) The result from the top cut with the whole right free surface is fixed. The direction of the x_1 is going into the plane of the cut surface.

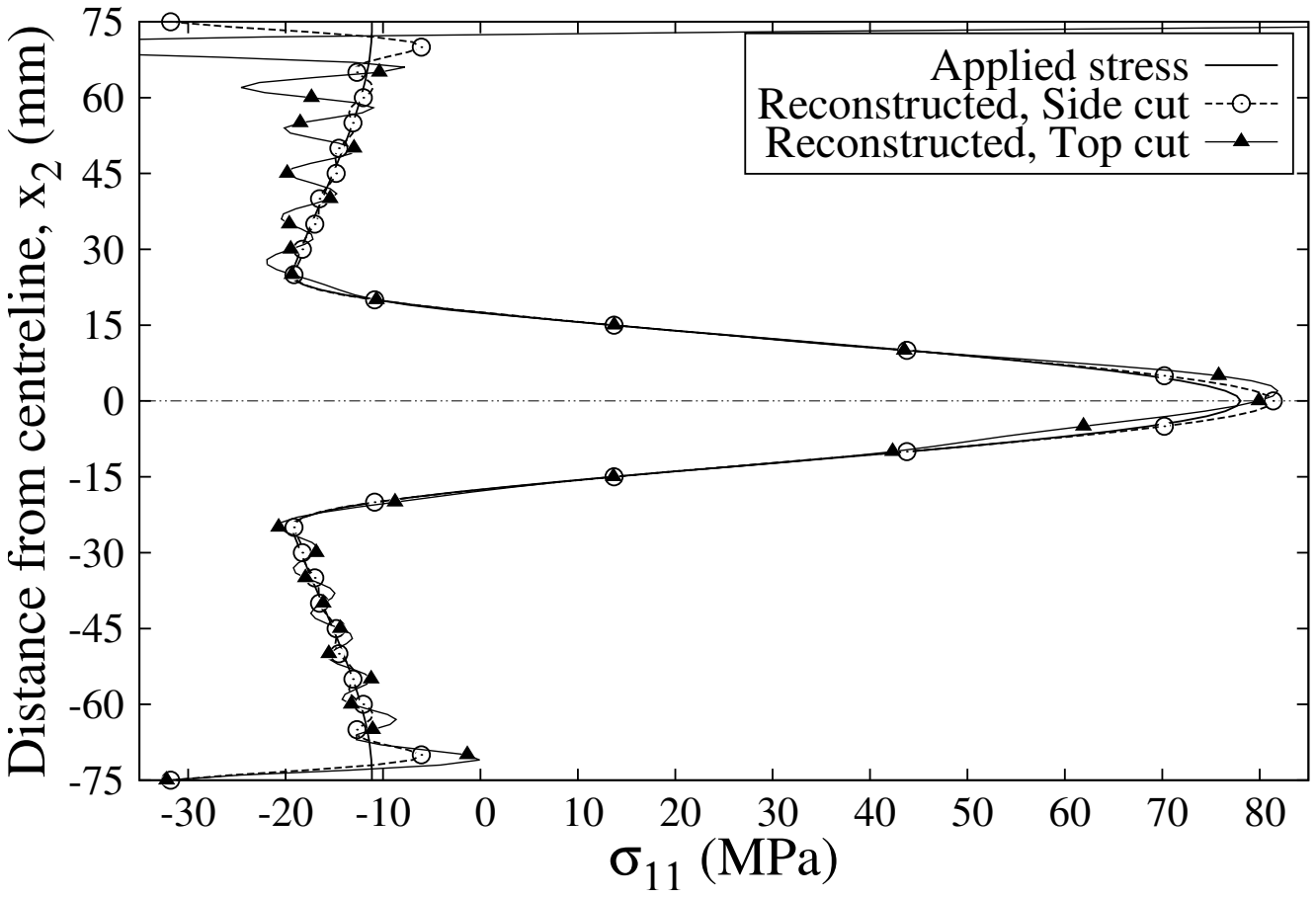

Figure 12: Residual stress fields, reconstructed from the FE relaxation displacements, obtained from the two cutting schedules, are compared with initial applied stress. Using data from the the top cut leads to higher harmonic noise, which is particularly high towards the edges of the specimen.

Fig. 12 shows the residual stress profile reconstructed from the two different cutting methods with a corner constraint. The relaxation displacement data were collected from the front surface, see Fig. 10(a). The residual stress reconstructed from the top cut suffers from higher harmonic noise. However, this might also be due to the constraint effect for short specimens.

This analysis supports findings from [31, 16]. For thin plates a side cut is preferable to a top cut, because a side cut causes less plasticity.

5. Experiments

Brief details of specimen preparation are given here. The full description is given in [20]. Several 216 mm × 150 mm × 3 mm plates were manufactured from aluminium alloy 5083-O ($\sigma_Y = 145$

MPa, UTS = 290 MPa), of which two were selected for this work. Each plate was cut into two parts by water jet at the centre of the width along the longitudinal direction. Advantages of the water jet technique are low heat generation and low specimen distortion [32]. The two parts were then welded at the Friction Processing Research Institute, Nelson Mandela Metropolitan University in South Africa on an MTS I-Stir PDS Friction stir welder. The specimen was welded under force control, with a spindle speed of 400 rpm and feed-rate of 200 mm/min using a shoulder and pin diameter of 22 and 5 mm.

5.1. Preparation

Accurate full-field measurement of the relaxation after the EDM cut is critical in the experiment. In this experiment, the relaxation was measured with 3D DIC. The specimen was clamped with four Aluminium bars (σ_Y = 503 MPa, UTS = 572 MPa). Two sets of bolted top and bottom bars are located 70 mm away from the midsection of the specimen where EDM cutting is carried out, see Fig. 13(a). The clamping bars are connected rigidly by two connecting bars to keep the two halves of the cut specimen together after the EDM cut. The upper connecting bar is removed for the top cut.

5.2. Optical system & surface preparation

The measurement of the relaxation was performed using Dantec Dynamics 3D DIC system [33]. The system consists of two 12-bit 2448 × 2050 pixel CCD cameras with zoom lenses and LED light illumination. Taking specimen symmetry into account, only half width of the specimen was recorded to achieve a higher displacement resolution. The field of view was 76 mm × 63 mm, and the DIC stereo parameters were: the angle of 18.87° and baseline of 116.34 mm. The spatial resolution was $31\mu m$/pixel. The accuracy was between 0.31 and 0.62 μ m/pixel based on the accuracy of sub-pixel resolution algorithms, typically between 0.02 to 0.01 pixel [34].

The accuracy of the DIC critically depends upon suitable surface preparation. In this work two challenges of surface preparation were faced: (1) the preservation of the surface during the EDM cutting and (2) creation of the suitable size of the random speckle pattern. During the EDM cutting the specimen is submerged in water and damage can be caused by the EDM wire

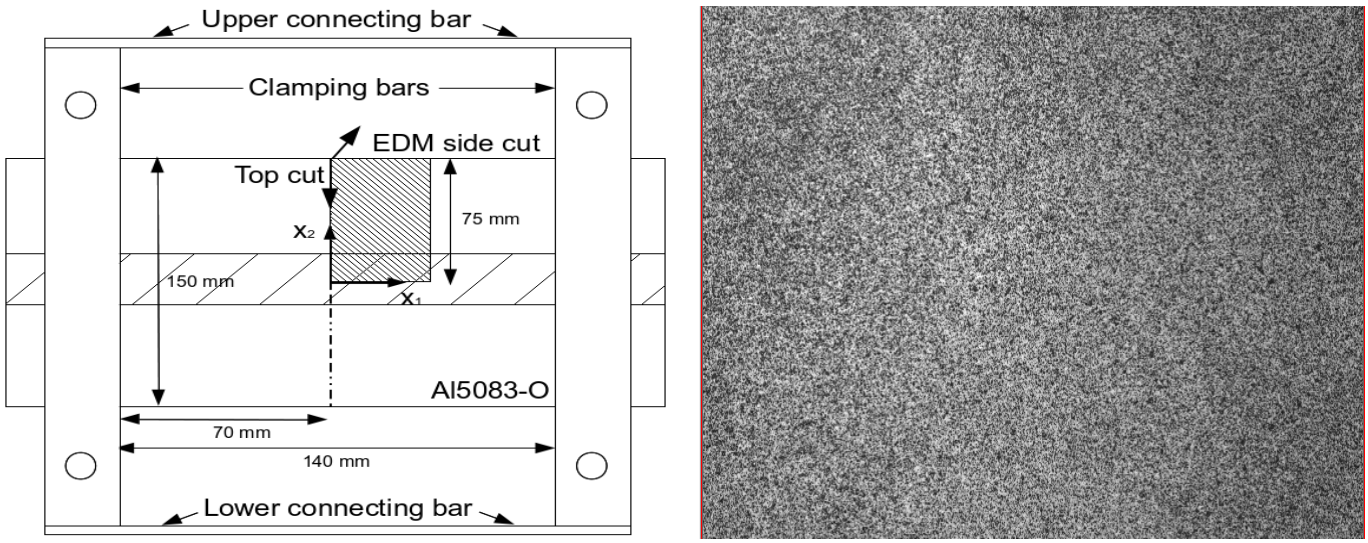

Figure 13: Layout of the specimen and the clamps. The rigid clamping and connecting bars have been employed to minimise rigid-body motion after the cut. EDM wire cutting was done along the dashed line. The fine hatched area indicates the area where the DIC data was collected. The upper side of connecting bar is removed for the top cut. (b) Surface pattern created with matt black and white spray paints. The field of view is approximately 71 $\times$ 63 mm^2, giving spatial resolution of 31 μ m/pixel.

to the pattern near the cut. The DIC pattern quality critically affects the displacement accuracy. A random uniform speckle pattern with 3-5 pixels per speckle is typically recommended for high resolution measurement of small displacements [35]. Matt black/white spray paint was found most effective in this work, see Fig. 13(b).

There is a trade-off between the quality and quantity of the measured data. Ideally, relaxation from the whole width of the specimen should be recorded. However, this cannot be done using the available current DIC system while maintaining high resolution. Therefore, relaxation data from only half the width of the specimen was recorded, see Fig. 13(a). The sensitivity analysis of Sec. 3 shows that good RS reconstruction can be expected at $x_2 \geq 0$, Sec. 3.2.

The EDM wire diameter was 0.25 mm. The wire speeds were 18.75 mm/min and 0.7 mm/min for the top and the side cuts respectively. The speeds were chosen to ensure the same material volume removal rate in both cases.

6. Results

The u_1 and u_2 displacement fields from both EDM cutting schedules are shown in Fig. 14. Generally, it is known that larger DIC subset sizes give more accurate average displacements, at the expense of not resolving sharp gradients. The optimum DIC subset and step size in this work were 35 and 25 pixels respectively, giving the displacement spatial resolution of 0.76 mm. There were a few spots where the DIC algorithm failed, perhaps due to surface pattern damage.

Fig. 14(a) and (b) shows that u_1 and u_2 decay slower than expected with x_1. In particular, high u_2 values away from the cut indicate that rigid body rotation might have occurred.

Fig. 14(c) shows the u_1 relaxation displacement for the top cut and Fig. 14(d) compares u_1 relaxation displacements near the cut from about $x_1 = 0.15$ to 1.67 mm for the top and the side cuts. Significant local distortion very close to the cut is seen in the top cut u_1 field. The magnitude of u_1 is much lower in the top cut than in the side cut. This is due to the plastic strain induced during the top cut [16], which leads to large errors in the reconstructed residual stress fields, see Fig. 15.

Fig. 15 compares the RS profiles from the top half width of the specimen, reconstructed from the measured relaxation displacement fields, compared with EDXRD [20]. The u_1 displacement

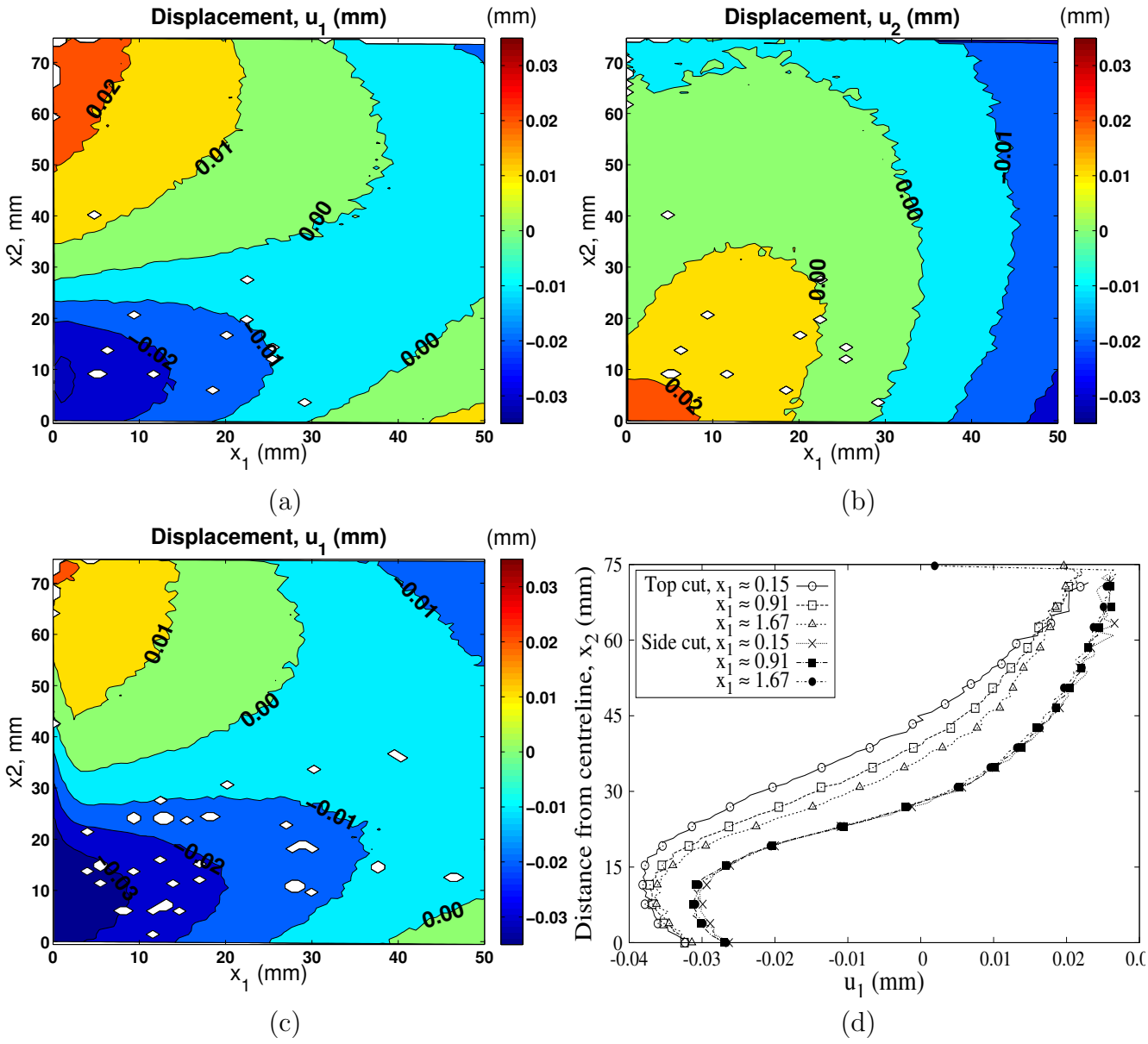

Figure 14: (a) and (b) u_1 and u_2 relaxation displacement fields from the side cut. $x_2 = 0$ is the centre weld line. White spots show areas where DIC failed to calculate displacement, perhaps due to damaged surface pattern. (c) u_1 relaxation displacement field from the top cut. (d) u_1 relaxation displacement profiles in the vicinity of the cutting edge. The magnitude of u_1 near the cut is lower in the top cut than that in the side cut. This is the likely effect of cutting induced plasticity in the top cut.

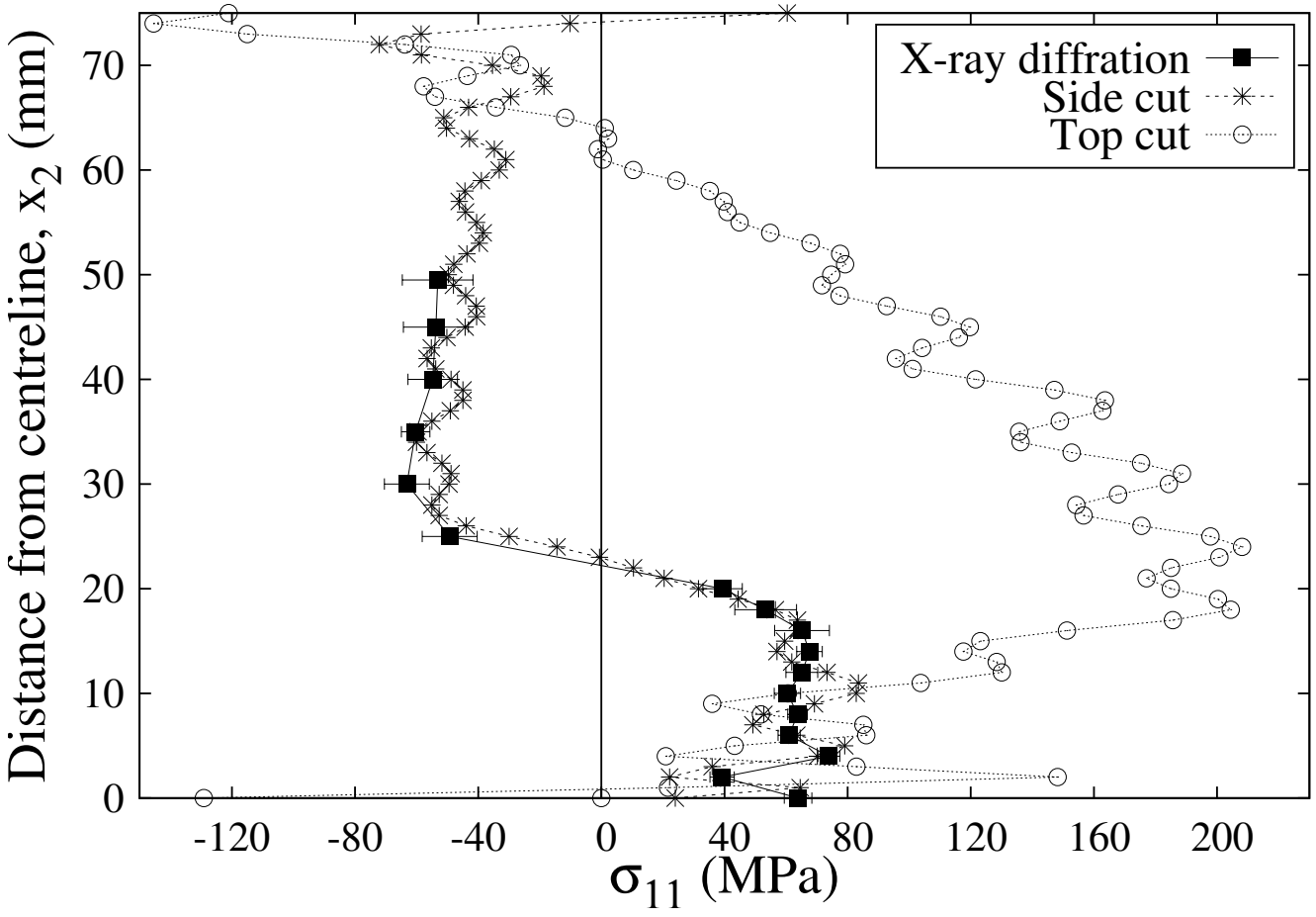

Figure 15: RS profiles, reconstructed from the measured relaxation displacement fields from the side (front) and the top cuts, are compared against EDXRD [20]. The RS profile from the side cut agrees very well with that from EDXRD, but that from the top cut does not.

field between $x_1 = 0$ to 5 mm was used for the residual stress reconstruction. The series limit was 15. For the side cut the agreement is very good. However, the RS reconstructed from the top cut shows poor agreement with the EDXRD result.

7. Concluding remarks

A detailed analysis of the sensitivity of the new side cut MSR method for measuring residual stresses in thin plates was carried out. A friction stir welded plate was used in this study. It has a symmetric RS field, with tension in the weld area and compression in the virgin material. Insufficient specimen length was shown cause errors in the reconstructed RS. For this RS field and the specimen shape, it is recommended to apply the method for specimens longer than the width. Relaxation in short specimens is sensitive to the level of constraint at the far edge of the plate. It is shown that constraining only the far edge corners is preferable to constraining the whole far edge, because this results in lower cutting induced plastic strain. The method was shown to be insensitive to omission of data from large areas of displacement field. However, it is very sensitive to in-plane rigid body rotation. Therefore rigid body compensation was implemented, which dramatically improved the quality of the reconstructed RS profile.

Although care was taken to implement the recommendations from the sensitivity analysis in the FSW plate experiment, some of those could not be fulfilled. The specimen length was shorter than $2c$. In addition, despite the use of clamping, some rigid body rotation seems to have occurred. This highlights the technical challenges of applying the method in practice. Despite these complications, the measured RS profile in a 3mm thick FSW Al 5083-O plate agreed very well with that from the EDXRD.

Direction of propagation of the cut was confirmed to affect stress redistribution and the amount of plastic flow on cutting. The side cut was shown to induce no plasticity on the front surface. The top cut does induce some plastic deformation on the front surface and thus invalidates the assumption that the relaxation displacements are related to the residual stress via an inverse elastic problem. This shows that induced-plasticity on the cut can be minimised by choosing suitable propagation of the cut. This conclusion might be applicable to some other MSR methods, where there is some freedom in how the cut is introduced.

A higher resolution 3D DIC system would allow collecting data from the whole specimen width, while maintaining a high spatial resolution. This would improve the stability of the method by increasing the amount of displacement data close to the cut.

8. Acknowledgements

This work was carried out using the computational facilities of the Advanced Computing Research Centre, University of Bristol - http://www.bris.ac.uk/acrc. The authors are indebted to Dr. Graeme Horne for providing the specimens and EDXRD data.

References

[1] A. Steuwer, M. J. Peel, P. J. Withers, Dissimilar friction stir welds in AA5083-AA6082: The effect of process parameters on residual stress, Material Science & Engineering A 441 (2006) 187–196. doi:10.1016/j.msea.2006.08.012.

[2] P. Staron, M. Koçak, S. Williams, A. Wescott, Residual stress in friction stir-welded Al sheets, Physica B: Condensed Matter 350 (1-3) (2004) 491–493. doi:10.1016/j.physb.2004.03.128.

[3] P. J. Webster, L. D. Oosterkamp, P. A. Browne, D. J. Hughes, W. P. Kang, P. J. Withers, G. B. M. Vaughan, Synchrotron X-ray residual strain scanning of a friction stir weld, Journal of Strain Analysis for Engineering Design 36 (2001) 61–70. doi:10.1243/0309324011512612.

[4] T. S. Jun, S. Y. Zhang, M. Golshan, M. Peel, D. Richards, A. M. Korsunsky, Synchrotron energy-dispersive X-ray diffraction analysis of residual strains around friction welds between dissimilar aluminium and nickel alloys, in: Stress Evaluation in Materials Using Neutrons and Synchrotron Radiation, Vol. 571-572 of Materials Science Forum, Trans Tech Publications, 2008, pp. 407–412. doi:10.4028/www.scientific.net/MSF.571-572.407.

[5] O. Hatamleh, A. DeWald, An investigation of the peening effects on the residual stresses in friction stir welded 2195 and 7075 aluminum alloy joints, Journal of Materials Processing Technology 209 (2009) 4822–4829. doi:10.1016/j.jmatprotec.2008.12.010.

[6] P. J. Withers, Residual stress and its role in failure, Reports on Progress in Physics 70 (12) (2007) 2211–2264.
URL http://stacks.iop.org/0034-4885/70/i=12/a=R04

[7] G. S. Schajer, M. B. Prime, Use of inverse solutions for residual stress measurements, Journal of Engineering Materials and Technology-Transactions of the ASME 128 (3) (2006) 375–382. doi:10.1115/1.2204952.

[8] G. S. Schajer, Measurement of non-uniform residual stresses using the hole-drilling method. Part I - Stress Calculation Procedures, Journal of Engineering Materials and Technology-Transactions of the ASME 110 (4) (1988) 338–343. doi:10.1115/1.3226059.

[9] R. Leggatt, D. Smith, Development and experimental validation of the deep hole method for residual stress measurement, The Journal of Strain Analysis for Engineering Design 31 (3) (1996) 177–186. doi:10.1243/03093247V313177.

[10] M. B. Prime, Residual stress measurement by successive extension of a slot: the crack compliance method, Applied Mechanics Reviews 52 (2) (1999) 75–96. doi:10.1115/1.3098926.

[11] W. Cheng, I. Finnie, Residual Stress Measurement and the Slitting Method, Springer, New York, 2007. doi:10.1007/978-0-387-39030-7.

[12] M. B. Prime, Cross-sectional mapping of residual stresses by measuring the surface contour after a cut, Journal of Engineering Materials and Technology 123 (2001) 162–168. doi:10.1115/1.1345526.

[13] G. S. Schajer, P. S. Whitehead, Hole drilling and ring coring, in: G. S. Schajer (Ed.), Practical residual stress measurement methods, John Wiley & Sons, 2013, pp. 29–64. doi:10.1002/9781118402832.

[14] W. Xu, J. Liu, H. Zhu, Analysis of residual stresses in thick aluminum friction stir welded butt joints, Materials & Design 32 (4) (2011) 2000–2005. doi:10.1016/j.matdes.2010.11.062.

[15] M. B. Prime, Measuring residual stress and the resulting stress intensity factor in compact tension specimens, Fatigue and Fracture of Engineering Materials and Structure 22 (3) (1999) 195–204. doi:10.1046/j.1460-2695.1999.00155.x.

[16] H. K. Kim, H. E. Coules, M. J. Pavier, A. Shterenlikht, Measurement of highly non-uniform residual stress fields with reduced plastic error, Experimental Mechanics 55 (2015) 1211–1224. doi:10.1007/s11340-015-0025-1.

[17] W. Woo, H. Choo, D. W. Brown, Z. Feng, P. K. Liaw, Angular distortion and through-thickness residual stress distribution in the friction-stir processed 6061-T6 aluminum alloy, Materials Science and Engineering: A 437 (1) (2006) 64–69. doi:10.1016/j.msea.2006.04.066.

[18] V. Richter-Trummer, E. Suzano, M. Beltrão, A. Roos, J. dos Santos, P. de Castro, Influence of the FSW clamping force on the final distortion and residual stress field, Materials Science and Engineering: A 538 (2012) 81–88. doi:10.1016/j.msea.2012.01.016.

[19] M. R. Hill, The slitting method, in: G. Schajer (Ed.), Practical residual stress measurement methods, John Wiley & Sons, 2013, p. 96. doi:10.1002/9781118402832.

[20] G. Horne, Elastic follow-up and the interaction between applied and residual stresses, Ph.D. thesis, University of Bristol (2013).

[21] I. A. Razumovskii, A. L. Shterenlikht, Determining the locally-nonuniform residual-stress fields in plane parts by the sectioning method, Journal of Machinery Manufacture and Reliability *C/C of* Problemy Mashinostroeniia i Nadezhnosti Mashin 4 (2000) 40–45.

[22] S. Timoshenko, J. N. Goodier, Theory of Elasticity, 3rd Edition, McGraw-Hill, 1970.

[23] A. N. Tiknonov, V. Y. Arsenin, Solutions of Ill-posed Problems, Wiley, 1977.

[24] S. A. Faghidian, A smoothed inverse eigenstrain method for reconstruction of the regularized residual fields, International Journal of Solids & Structures 51 (2014) 4427–4434. doi:10.1016/j.ijsolstr.2014.09.012.

[25] S. A. Faghidian, Inverse determination of the regularized residual stress and eigenstrain fields due to surface peening, Journal of Strain Analysis for Engineering Design 50 (2015) 84–91. doi:10.1177/0309324714558326.

[26] LAPACK - Linear Algebra PACKage, Version 3.6.0, http://www.netlib.org/lapack (2015).

[27] Dassault Systèmes, Abaqus FEA, http://www.simulia.com/products/abaqus_fea.html (HTML) (2009).

[28] G. S. Schajer, M. Steinzig, Full-field calculation of hole drilling residual stresses from electronic speckle pattern interferometry data, Experimental Mechanics 45 (2005) 526–532. doi:10.1007/BF02427906.

[29] M. B. Prime, Plasticity effects in incremental slitting measurement of residual stresses, Engineering Fracture Mechanics 77 (2010) 1552–1566. doi:10.1016/j.engfracmech.2010.04.031.

[30] S. H. Shin, FEM analysis of plasticity-induced error in measurement of welding residual stress by the contour method, Journal of Materials Science and Technology 19 (10) (2005) 1885–1890. doi:10.1007/BF02984267.

[31] H. K. Kim, M. J. Pavier, A. Shterenlikht, Plasticity and stress heterogeneity influence on mechanical stress relaxation residual stress measurements, in: Proceedings of 9th European Conference on Residual Stresses, 7-10 July 2014, Troyes, France, 2014.

[32] S. Kalpakjian, S. R. Schmid, H. Musa, Manufacturing engineering and technology, 6th Edition, Prentice Hall, 2010.

[33] Dantec Dynamics, ISTRA 4D Software Manual Q-400 system (2012).

[34] B. Pan, H.-m. Xie, B.-q. Xu, F.-l. Dai, Performance of sub-pixel registration algorithms in digital image correlation, Measurement Science and Technology 17 (6) (2006) 1615–1621. doi:10.1088/0957-0233/17/6/045.

[35] P. Reu, Hidden Components of DIC: Calibration and Shape Function - Part 1, Experimental Techniques 36 (2) (2012) 3–5. doi:10.1111/j.1747-1567.2012.00821.x.